remote sensing

MDPI

Article

A Study of NOAA-20 VIIRS Band M1 (0.41 μm) Striping over Clear-Sky Ocean

Wenhui Wang [1,*], Changyong Cao [2], Slawomir Blonski [3] and Xi Shao [1]

[1] Cooperative Institute for Satellite Earth System Studies (CISESS), University of Maryland, College Park, MD 20740, USA; xi.shao@noaa.gov
[2] National Oceanic and Atmospheric Administration (NOAA)/National Environmental Satellite, Data, and Information Service (NESDIS)/Center for Satellite Applications and Research (STAR), College Park, MD 20740, USA; changyong.cao@noaa.gov
[3] Earth Resource Technology (ERT) Inc., Laurel, MD 20707, USA; slawomir.blonski@noaa.gov
* Correspondence: wenhui.wang@noaa.gov

Abstract: The Visible Infrared Imaging Radiometer Suite (VIIRS) onboard the National Oceanic and Atmospheric Administration-20 (NOAA-20) satellite was launched on 18 November 2017. The on-orbit calibration of the NOAA-20 VIIRS visible and near-infrared (VisNIR) bands has been very stable over time. However, NOAA-20 operational M1 (a dual gain band with a center wavelength of 0.41 μm) sensor data records (SDR) have exhibited persistent scene-dependent striping over clear-sky ocean (high gain, low radiance) since the beginning of the mission, different from other VisNIR bands. This paper studies the root causes of the striping in the operational NOAA-20 M1 SDRs. Two potential factors were analyzed: (1) polarization effect-induced striping over clear-sky ocean and (2) imperfect on-orbit radiometric calibration-induced striping. NOAA-20 M1 is more sensitive to the polarized lights compared to other NOAA-20 short-wavelength bands and the similar bands on the Suomi NPP and NOAA-21 VIIRS, with detector and scan angle-dependent polarization sensitivity up to ~6.4%. The VIIRS M1 top of atmosphere radiance is dominated by Rayleigh scattering over clear-sky ocean and can be up to ~70% polarized. In this study, the impact of the polarization effect on M1 striping was investigated using radiative transfer simulation and a polarization correction method similar to that developed by the NOAA ocean color team. Our results indicate that the prelaunch-measured polarization sensitivity and the polarization correction method work well and can effectively reduce striping over clear-sky ocean scenes by up to ~2% at near nadir zones. Moreover, no significant change in NOAA-20 M1 polarization sensitivity was observed based on the data analyzed in this study. After the correction of the polarization effect, residual M1 striping over clear-sky ocean suggests that there exists half-angle mirror (HAM)-side and detector-dependent striping, which may be caused by on-orbit radiometric calibration errors. HAM-side and detector-dependent striping correction factors were analyzed using deep convective cloud (DCC) observations (low gain, high radiances) and verified over the homogeneous Libya-4 desert site (low gain, mid-level radiance); neither are significantly affected by the polarization effect. The imperfect on-orbit radiometric calibration-induced striping in the NOAA operational M1 SDR has been relatively stable over time. After the correction of the polarization effect, the DCC-based striping correction factors can further reduce striping over clear-sky ocean scenes by ~0.5%. The polarization correction method used in this study is only effective over clear-sky ocean scenes that are dominated by the Rayleigh scattering radiance. The DCC-based striping correction factors work well at all radiance levels; therefore, they can be deployed operationally to improve the quality of NOAA-20 M1 SDRs.

Academic Editor: Stephan Havemann

Received: 18 November 2024
Revised: 19 December 2024
Accepted: 26 December 2024
Published: 28 December 2024

Citation: Wang, W.; Cao, C.; Blonski, S.; Shao, X. A Study of NOAA-20 VIIRS Band M1 (0.41 μm) Striping over Clear-Sky Ocean. *Remote Sens.* **2025**, *17*, 74. https://doi.org/10.3390/rs17010074

Keywords: Visible Infrared Imaging Radiometer Suite (VIIRS); NOAA-20; sensor data records (SDR); M1; striping; Rayleigh scattering; polarization effect; polarization sensitivity; clear-sky ocean; deep convective clouds (DCC); Libyan-4; polarization correction; striping correction

1. Introduction

The Visible Infrared Imaging Radiometer Suite (VIIRS) is currently onboard the National Oceanic and Atmospheric Administration-21 (NOAA-21, launched on 10 November 2022), the NOAA-20 (launched on 18 November 2017), and the Suomi National Polar-orbiting Partnership (S-NPP, launched on 28 October 2011) satellites [1–3]. VIIRS is equipped with five imaging bands (I-bands, 375 m at nadir), 16 moderate resolution bands (M-bands, 750 m at nadir), and one Day/Night Band (DNB, 750 m). VIIRS has 14 reflective solar bands (RSB), including three I-bands (I1–I3) and 11 M-bands (M1–M11). Each VIIRS M-band has 16 detectors, while each I-band has 32 detectors. NOAA-21, NOAA-20, and S-NPP VIIRS RSB sensor data records (SDR) are valuable for a wide variety of environmental and climate data records, such as ocean color, cloud and aerosol properties, vegetation indices, and surface reflectance/albedo.

VIIRS is a scanning radiometer with a rotating telescope assembly (RTA) that rotates 360° to collect signals from the Earth view (EV) port and the onboard calibrators, including the solar diffuser (SD), solar diffuser stability monitor (SDSM), onboard calibrator blackbody, and space view port. Then, a half-angle mirror (HAM), which rotates at half the speed of the RTA, directs the output signals from the RTA to the aft optics assembly. The light is then spectrally and spatially separated by dichroic beam splitters and directed to three separate focal plane assemblies (FPA): the visible/near-infrared (VisNIR) FPA, the shortwave/midwave infrared FPA, and the longwave infrared FPA. The on-orbit calibration of VIIRS RSB is complex, depending on prelaunch calibration parameters and on-orbit calibration scaling factors (F-factors). VIIRS RSB F-factors are derived using onboard solar calibration and complemented by vicarious calibrations such as lunar calibration as well as Pseudo-Invariant Calibration Site (PICS) and deep convective cloud (DCC) observations.

NOAA-20 VIIRS VisNIR bands (M1–M7 and I1–I2) SDRs became available on 13 December 2017. During the past six and half years, the on-orbit detector responsivity degradation of NOAA-20 VIIRS VisNIRs has been very small. NOAA-20 operational SDRs for VisNIR have been stable after it achieved validated maturity status on 28 April 2018, with trends of ~0.1%/year or less [4–7]. The Global Space-based Inter-Calibration System (GSICS) recommended NOAA-20 VIIRS RSBs as the calibration reference in 2021 [8]. A remaining issue is that persistent striping has been observed in the M1 SDR over clear-sky ocean and its downstream ocean color water leaving radiance product (nLW_411) since the beginning of the mission. No obvious striping is observed in other NOAA-20 VisNIR SDRs or in their corresponding ocean color products. Moreover, the NOAA-20 M1 striping over clear-sky ocean is strongly scene dependent, varying with solar and sensor viewing geometries.

Unlike S-NPP and NOAA-21 VIIRS, NOAA-20 VIIRS shorter wavelength VisNIR bands (M1–M4) are more sensitive to polarized light according to prelaunch test results [9–13]. Table 1 summarizes VIIRS bands M1–M4 polarization sensitivity specifications and maximum prelaunch characterized detector level polarization sensitivity for NOAA-20, S-NPP, and NOAA-21. Among all NOAA-20 VisNIR bands, M1 has the highest polarization sensitivity (up to ~6.4%), which is strongly detector- and scan angle-dependent. As a result, polarization effect introduces larger striping in the M1 SDRs compared to other VisNIR

bands. Polarization effect is not corrected at the SDR level. Therefore, the striping due to the polarization effect must first be corrected to investigate the root causes of striping in NOAA-20 M1 over clear-sky ocean. Moreover, M1 is a dual-gain band, with ocean color retrievals using low radiances (at high gain). On the other hand, vicarious calibrations are usually performed at higher radiances. The on-orbit calibration performance may not be the same at different radiance levels. Lei et al. [14] presents the NOAA-20 VIIRS VisNIR striping for unpolarized light and its mitigation in the NASA level 1B data (equivalent to SDR). However, NOAA and NASA NOAA-20 VIIRS SDRs are calibrated independently. Moreover, the impacts of the striping correction over clear-sky ocean have not been studied so far. Further analyses are required to better understand the observed striping over clear-sky ocean in the operational NOAA-20 M1 SDRs.

Table 1. VIIRS bands M1–M4 polarization sensitivity specifications and maximum prelaunch characterized detector level polarization sensitivity for NOAA-20, S-NPP, and NOAA-21 bands M1–M4, within ±45° scan angle (unit: %).

Band	Center Wavelength (μm)	Specification	NOAA-20	S-NPP	NOAA-21
M1	0.411	3	6.4	2.6	4.8
M2	0.445	2.5	4.5	1.9	1.7
M3	0.489	2.5	3.1	1.2	1.3
M4	0.556	2.5	4.3	1.4	1.2

This study analyzes the potential root causes of NOAA-20 VIIRS M1 striping over clear-sky ocean in the NOAA operational processing. First, the polarization effect was simulated using a vectorized radiative transfer model. A polarization correction method similar to the method used by the NOAA ocean color science team was used to correct the polarization effect. Then, the striping induced by VIIRS on-orbit radiometric calibration errors was analyzed using an improved DCC-based method and evaluated over the Libya-4 desert site. Finally, the effectiveness of the DCC-based striping correction factors over clear-sky ocean scenes was evaluated and discussed.

This paper is organized as follows. NOAA-20 VIIRS M1 SDRs and methods for quantifying striping are described in Section 2. Section 3 focuses on the polarization effect over clear-sky ocean and the correction of polarization effect-induced striping for NOAA-20 M1. Section 4 presents the DCC-based method for characterizing M1 striping due to imperfect radiometric calibration. The impacts of polarization and the DCC-based striping corrections on M1 clear-sky ocean are given and discussed in Section 5. Section 6 concludes this study.

2. NOAA-20 VIIRS M1 SDR and Method for Quantifying Striping

2.1. NOAA-20 VIIRS M1 SDRs

NOAA-20 VIIRS operational M1 SDRs were used in this study. Different from S-NPP VIIRS, the on-orbit detector responsivity degradations of NOAA-20 VIIRS RSBs have been very small according to the onboard SD calibration and vicarious calibrations including lunar calibration and the DCC technique [7,15]. Band M1, as well as other RSBs, had been calibrated using constant detector-, HAM-side-, and gain stage-dependent F-factors from 27 April 2018 to 4 November 2021. The NOAA-20 VisNIR F-factors were updated on 4 November 2021 to compensate for the small long-term trends observed in the lunar and DCC time series, with a band-averaged trend of 0.03%/year applied to M1 to correct its long-term degradation [7].

The operational NOAA-20 VIIRS VisNIR SDRs have been very stable since 27 April 2018. Figure 1 shows monthly DCC time series for bands M1–M4 in the NOAA operational processing. The trends are less than 0.06%/year for all bands. The trend of M1 monthly DCC reflectance is −0.01%/year, within a 95% confidence interval of 0.04%/year. We also evaluated the M1 calibration stability over Libya-4 and Dome-C sites, and similar in-significant trends were observed.

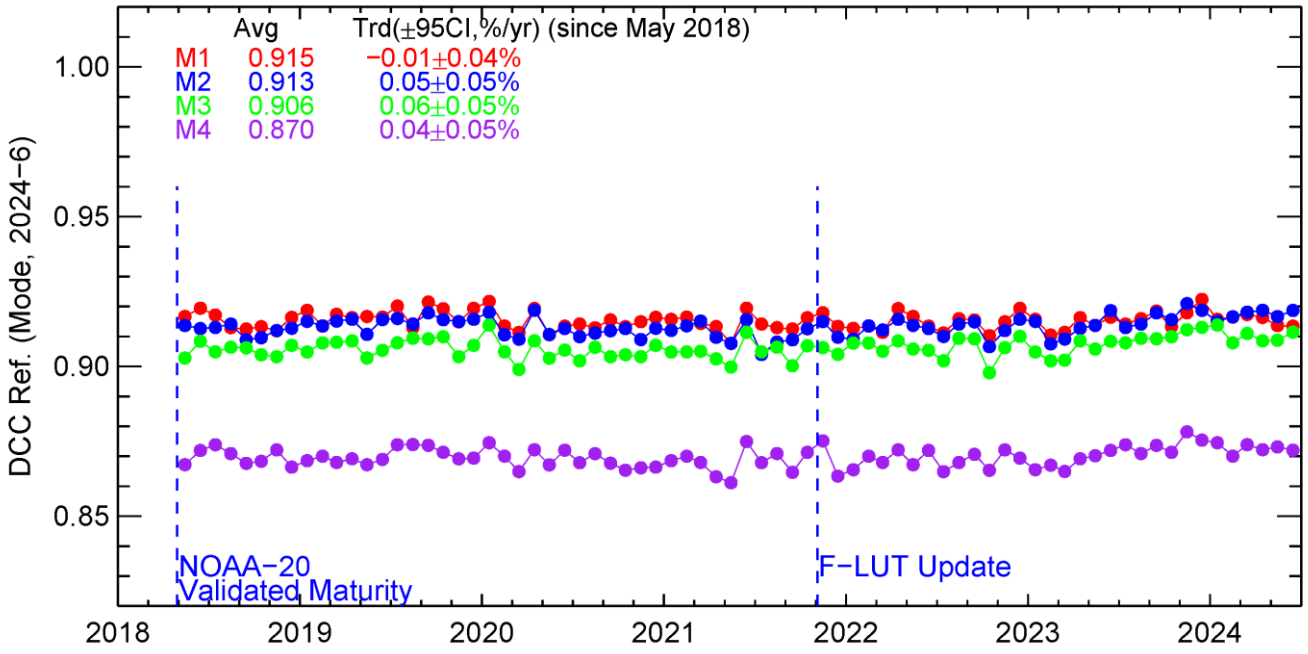

Figure 1. Monthly DCC reflectance (mode) time series for NOAA-20 VIIRS bands M1–M4 from May 2018 to June 2024.

Figure 2a shows the NOAA-20 M1 detector-level relative spectral response (RSR) functions. The M1 detector-level RSR differences are small (about 0.1%), suggesting that the M1 striping is unlikely caused by the detector-level RSR differences. In on-orbit calibration, differences in the detectors and HAM-side-dependent F-factors are derived based on prelaunch C-coefficients and on-orbit SD calibration. The differences in the detector, HAM-side, and gain-stage level M1 F-factors have remained nearly constant for both HG and LG since the beginning of the NOAA-20 mission. Figure 2b shows the operational M1 F-factors on 31 December 2023. In addition, the HAM-side differences for HG and LG F-factors are similar, both about 0.4%. VIIRS on-orbit calibration is complex, and uncertainty exists in the SD calibration results. Although the long-term trend in the M1 SDRs have been mitigated by combined lunar and DCC calibrations, no detector level vicarious calibration results have been applied to the operations so far. Potential residual errors in the SD-derived detector and HAM-side level F-factors may introduce striping in the M1 SDRs.

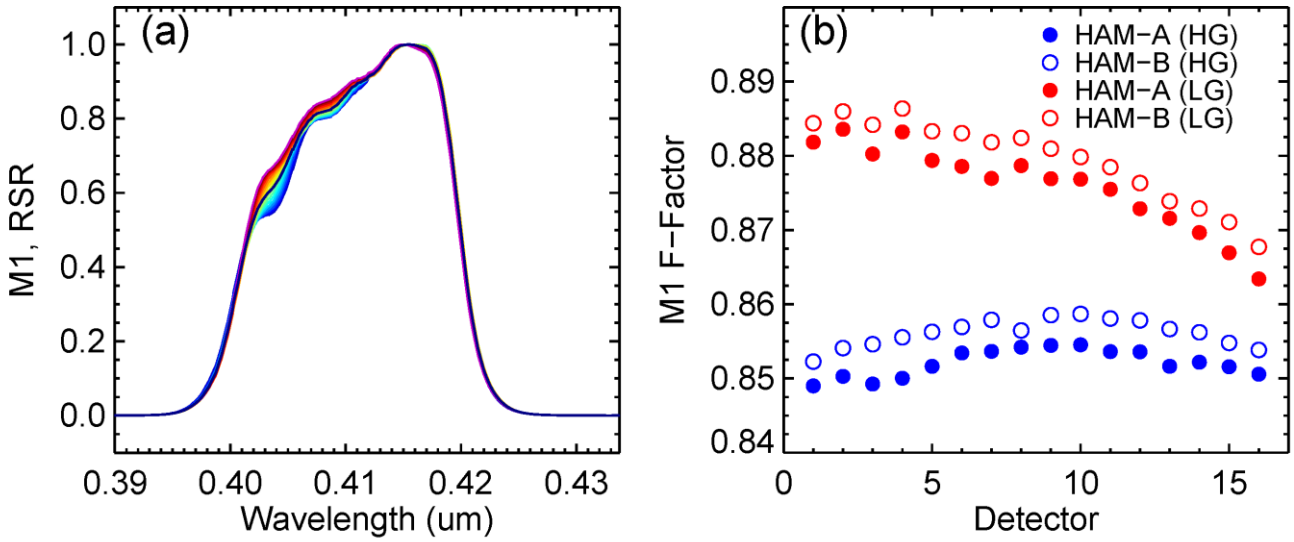

Figure 2. NOAA-20 M1 (**a**) detector level relative response (RSR, represented by different colors) functions and (**b**) operational F-factors on 31 December 2023 (right).

2.2. Method for Quantifying Striping in the VIIRS SDRs

Besides visual examinations, a quantitative method is needed to estimate the magnitude of striping in NOAA-20 M1 SDRs, especially when striping is relatively small. In this study, striping is quantified over a uniform rectangular area of interests (AOI) using a cumulative histograms method. First, a uniform area of interest (AOI) with an equal number of good quality pixels for each HAM side and detector is selected. Then, normalized cumulative histograms are calculated for each HAM side and detector:

$$H_{det,ham}(i) = \frac{1}{N_{det,ham}} \sum_{b=1}^{i} m_{b,det,ham} \quad (1)$$

where *det* is detector (1–16 for M-bands); *ham* is HAM-side (h = 0,1, for HAM-A and HAM-B, respectively); *b* is reflectance bin (b = 1,. . ., n, n represents the total number of reflectance bins, determined empirically); $m_{b,det,ham}$ is the histogram data for reflectance bin *b*, detector *det*, and HAM-side *ham*; $N_{det,ham}$ is the AOI's total number of pixels for HAM-side *ham* and detector *det*; and $H_{det,ham}(i)$ is the normalized cumulative histogram value for reflectance bins from 1 to *i*.

After normalized cumulative histograms ($H_{det,ham}(i)$) for each detector and HAM side are calculated, they are interpolated to 10 fixed H values from 0 to 1.0, with a step of 0.1. HAM-side and detector-level reflectance divergence at each H value is defined as the horizontal distance (reflectance difference) between the detector and HAM side with maximum and minimum reflectance. Striping index (*SI*) is defined as the averaged percentage of reflectance divergence at H values from 0.1 to 1.0:

$$SI\ (\%) = \frac{\sum_{h=0.1}^{1.0} \left\{ \begin{array}{c} \max\limits_{\substack{det=1\ldots16 \\ ham=0,1}} R(det,ham,h) - \min\limits_{\substack{det=1\ldots16 \\ ham=0,1}} R(det,ham,h) \end{array} \right\} dh}{\overline{R_{AOI}}} \cdot 100 \quad (2)$$

where *SI* is the striping index (unit: percent); h represents cumulative histogram values (h = 0.1 to 1.0, increased by dh = 0.1); $R(det, ham, h)$ is the detector- and HAM-side-dependent reflectance at h value, interpolated using $H_{det,ham}(i)$ values derived by

Equation (1); and $\overline{R_{AOI}}$ is the averaged reflectance of the entire AOI. Equations (1) and (2) can also be applied to the radiance domain. In this study, the striping index is calculated using M1 reflectance for convenience.

3. Polarization Effect-Induced Striping in NOAA-20 VIIRS M1 SDR over Clear-Sky Ocean

The polarization effect in the VIIRS SDRs depends on both the polarization sensitivity of the instrument and the polarization of the incoming light [16,17]. Sunlight coming directly from the sun, whose electric field has a random distribution in the plane perpendicular to the direction of propagation, is unpolarized. However, sunlight passing through the atmosphere and being reflected from the Earth scenes can become partially polarized, due to Rayleigh Scattering from the atmosphere, surface reflection (such as sun glint from the ocean surface), aerosol scattering, and other effects. As sunlight enters Earth's atmosphere, it interacts with air molecules, predominantly nitrogen and oxygen, causing Rayleigh scattering. Rayleigh Scattering is wavelength-dependent, inversely proportional to the fourth power of the wavelength. Therefore, shorter wavelengths are scattered more than longer wavelengths. NOAA-20 M1 has larger polarization sensitivities (see Table 1) that are strongly detector- and scan angle-dependent, hence introducing striping into the SDR images. To study the root causes of NOAA-20 M1 striping over clear-sky ocean, the Rayleigh Scattering-induced polarization effects must be first characterized and corrected.

3.1. Simulation of Rayleigh Scattering Effect over Clear-Sky Ocean

Over clear-sky ocean surfaces, away from sun-glint regions, top of atmosphere (TOA) radiance observed by a satellite instrument, such as VIIRS, is dominated by Rayleigh Scattering. Assuming that the polarization caused by aerosol scattering and surface reflection is negligible, the polarization effect can be well described by considering Rayleigh Scattering only. Polarized light can be described using a Stokes vector I:

$$\mathrm{I} = \begin{pmatrix} I \\ Q \\ U \\ V \end{pmatrix} \tag{3}$$

where I is the radiance that would be measured with a detector insensitive to the polarization state of the light; Q is horizontal-vertical linear polarization; U is $\pm 45^\circ$ linear polarization; and V is circular polarization. Over a clear-sky ocean, contributions from circular polarization, aerosol scattering, and surface reflection are small. The degree of polarization in TOA reflectance is dominated by the degree of linear polarization (*DoLP*):

$$DoLP = \frac{\sqrt{Q^2 + V^2}}{I^2} \tag{4}$$

In this study, Stokes vector components over clear-sky ocean were simulated using NOAA-20 VIIRS M1 band-averaged RSR and the Second Simulation of a Satellite Signal in the Solar Spectrum Vector Code, version 1.1 (6SV). Over clear-sky ocean, M1 TOA radiance varies strongly with solar zenith angle (SZA), sensor viewing zenith angle (VZA), solar azimuth angle (SAA), and sensor viewing azimuth angle (VAA). In addition, ocean surface-reflected radiance is also affected by surface roughness (wind speed) and surface pressure [18,19]. In this study, Stokes vectors were simulated at SZA from 0° to 88° (with an increment of 2°), at SAA from 0° to 360° (with an increment of 10°), at VZA from 0° to 70° (with an increment of 2°), and at VAA from 0° to 360° (with an increment of 10°), with wind speeds of 0.0, 0.1, 1.9, 4.2, 7.5, 11.7, 16.8, 22.9, and 29.5 m/s [19]. An aerosol optical

thickness value of 0.05 (at 550 nm) and a surface pressure of 1013.5 hPa were used during the simulation. A LUT table was generated to store the 6SV simulated Stokes vectors at representative SZA, SAA, VZA, VAA, and wind speeds.

Stokes vectors for given VIIRS observations were interpolated using the 6SV simulated LUT, solar and viewing geometries from the VIIRS geolocation product, and the Modern-Era Retrospective Analysis for Research and Applications, Version 2 (MERRA-2) data. Specifically, MERRA-2 1-h instantaneous product (0.625° × 0.5° spatial resolution) [20] was used to interpolate the wind speed and surface pressure at NOAA-20 VIIRS observation locations and times. The surface pressure effect on the TOA Rayleigh radiance was accounted for using a method given in [18]. An example of Stokes vectors and DoLP for a NOAA-20 VIIRS M1 granule on 9 January 2024 20:36–20:38 UTC (Pacific Coast, latitude: 29.27°, longitude: −116.95°) was given in Figure 3. The Stokes vectors for individual pixels were interpolated using the 6SV simulated LUT, by assuming that all pixels are clear-sky observations. The vertical features observed in the center of Figure 3b,c were caused by the rapid change in relative azimuth angle (RAA = SAA − VAA) at near nadir observations.

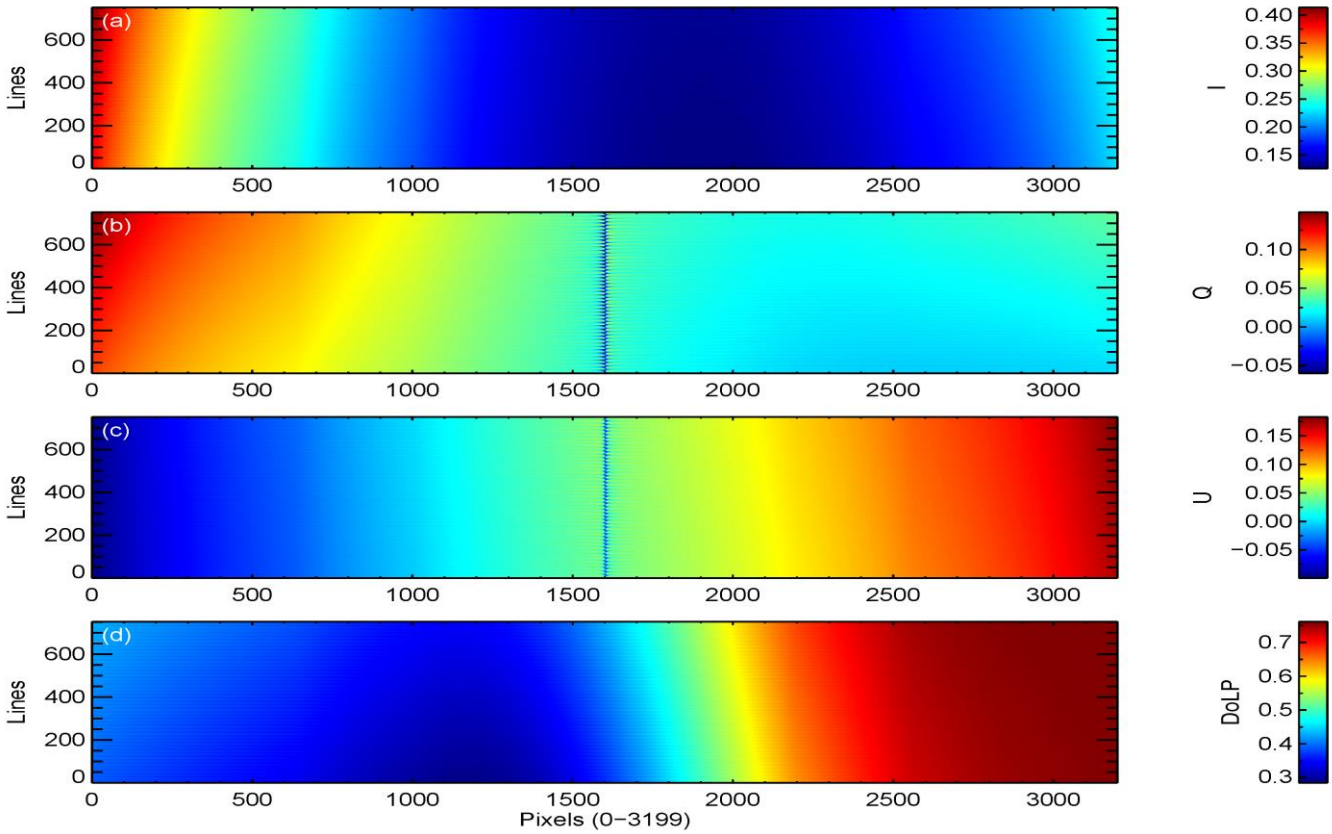

Figure 3. Example of 6SV simulated Stokes vectors (**a**) *I*, (**b**) *Q*, (**c**) *U*, and (**d**) DoLP for a NOAA-20 VIIRS M1 granule on 9 January 2024 20:36–20:38 UTC (Pacific Coast, latitude: 29.27°, longitude: −116.95°).

Figure 4 shows DoLP as functions of SZA, VZA, and RAA at surface pressure of 1013.5 hPa and wind speed of 5 m/s. DoLPs were calculated with Stokes vectors interpolated using 6SV simulated values. It can be observed that DoLP in M1 TOA radiance/reflectance varies strongly with solar and viewing geometries, from 0 to ~70%. DoLPs usually increase with SZA and VZA. Moreover, DoLPs are most pronounced in the forward scattering direction (RAA = 180°), while they are much smaller in the backward scattering direction (RAA = 0°).

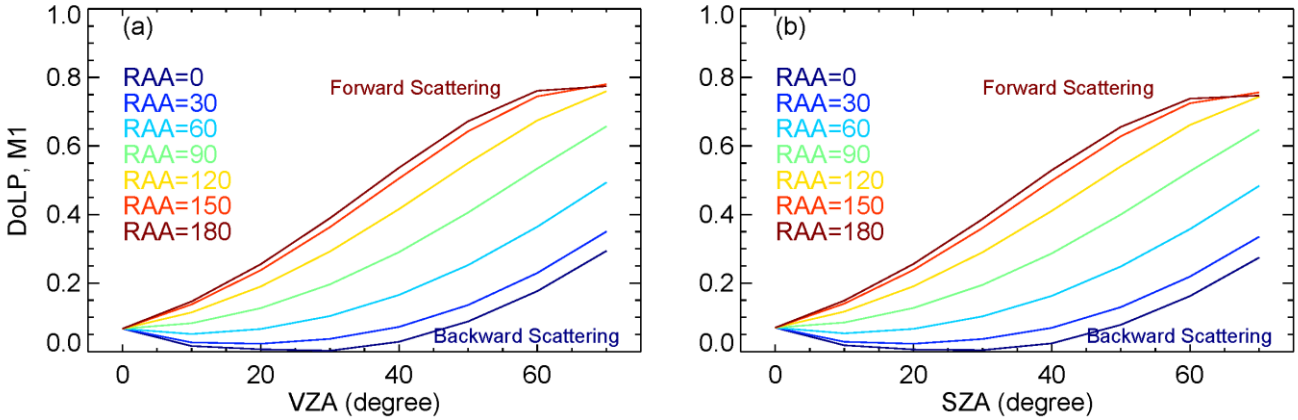

Figure 4. 6SV simulated degree of linear polarization (DoLP, unitless) over clear-sky ocean at surface pressure of 1013.5 hPa and wind speed of 5 m/s: (**a**) DoLP as functions of view zenith angle (VZA) and relative azimuth angle (RAA) at solar zenith angle (SZA) of 22.5°; (**b**) DoLP as functions of SZA and RAA at VZA of 22.5°.

The magnitude of DoLP due to Rayleigh Scattering can be more elegantly represented as a function of scattering angle (SA) [21], which is defined as follows [22]:

$$cos\gamma = \sin\theta_s \sin\theta_v \cos(\varphi_s - \varphi_v) + \cos\theta_s \cos\theta_v \quad (5)$$

where γ is the scattering angle; θ_s is SZA; θ_v is VZA; φ_s is SAA; and φ_v is VAA. Figure 5 shows DoLP as a function of the scattering angle for NOAA-20 M1. It can be observed that DoLP peaks at ~90° scattering angle and decreases toward 0 and 180° scattering angles.

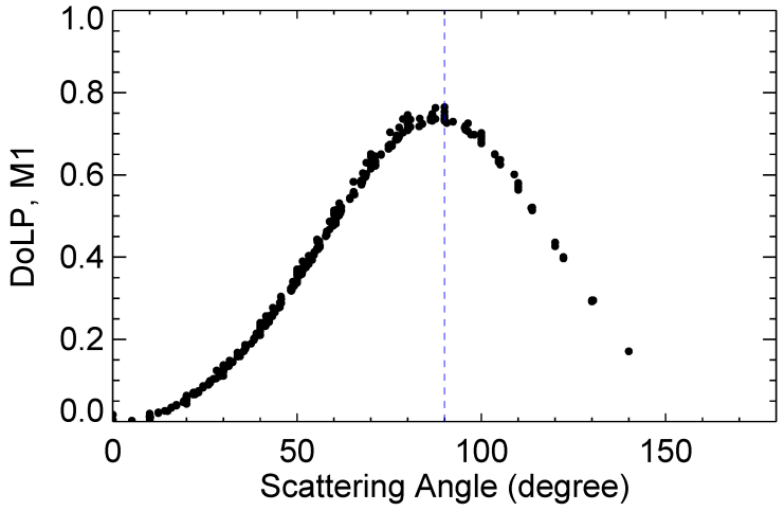

Figure 5. 6SV simulated DoLP (black dots) for NOAA-20 M1 over clear-sky ocean as a function of scattering angle, at a surface pressure of 1013.5 hPa and a wind speed of 5 m/s. The blue vertical dash line marks the 90° scattering angle.

3.2. M1 Prelaunch Polarization Sensitivity

VIIRS instrument polarization sensitivity for VisNIR bands was characterized during prelaunch tests. Details of NOAA-20 VIIRS polarization performance are given in previous studies [9,13]. Figure 6 shows NOAA-20 M1 detector- and HAM-side-dependent polarization sensitivity and phase angles at representative scan angles. The polarization sensitivity of NOAA-20 M1 is strongly detector- and scan angle-dependent. The polarization sensitivity also varies with the HAM sides, but the differences between the two HAM sides are relatively small. Table 1 compares VIIRS polarization sensitivity specification and

prelaunch characterization results for NOAA-20, NOAA-21, and S-NPP shorter wavelength bands (M1–M4). The polarization sensitivity of NOAA-20 M1–M4 is much higher than that of S-NPP and NOAA-21. Moreover, NOAA-20 M1–M4 did not meet the requirements, and a performance waiver was granted prelaunch.

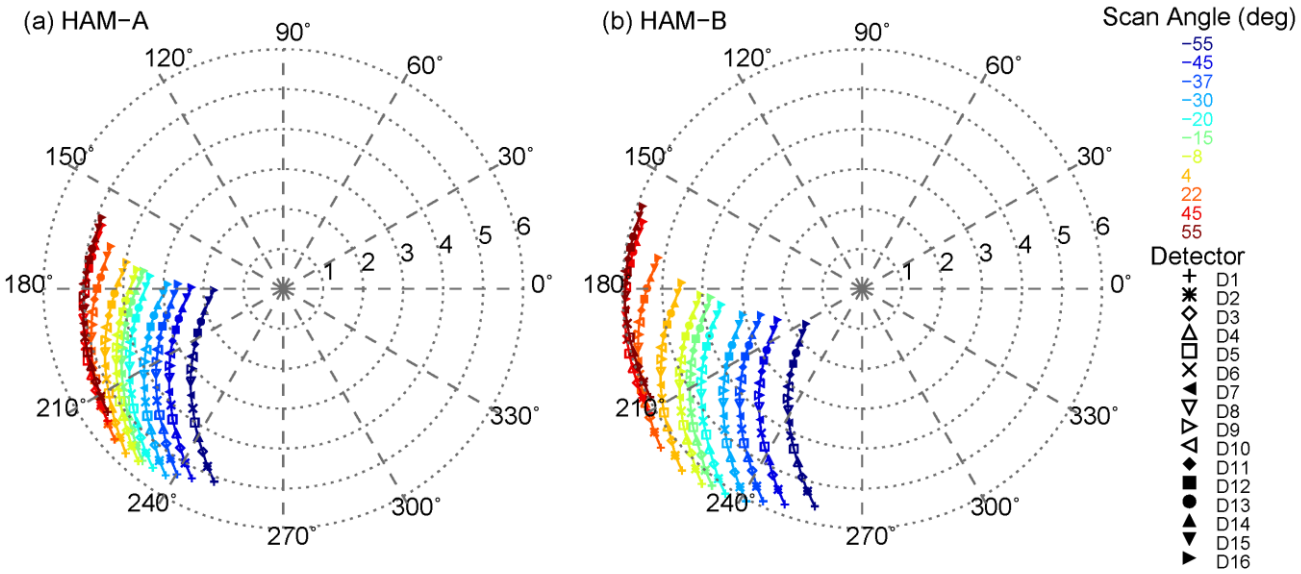

Figure 6. Polar plots of NOAA-20 VIIRS M1 prelaunch polarization sensitivity and phase angle at different scan angles for (**a**) HAM-A and (**b**) HAM-B. Polarization sensitivity (unit: percent) is represented by the length of a vector on the polar plot, while polarization phase angle is represented by the direction of the vector. Scan angle is represented by different colors; detector is represented by different symbols.

3.3. Method of Polarization Correction over Clear-Sky Ocean

In this study, the Rayleigh scattering-induced polarization effect was estimated and corrected using a method similar to those used by the NOAA ocean color science team [16], which has a heritage from MODIS ocean color polarization correction [23]. The following are the equations for correcting the polarization effect in NOAA-20 M1 SDRs:

$$R_{EV} = R_{EV}^{SDR} C_{pl} \tag{6}$$

$$C_{pl} = 1 + m_{12} q + m_{13} u \tag{7}$$

$$q = \frac{Q}{I} \; u = \frac{U}{I} \tag{8}$$

$$m_{12} = a\cos(2\delta) \tag{9}$$

$$m_{13} = a\sin(2\delta) \tag{10}$$

where R_{EV} is the TOA reflectance after the correction of the polarization effect; R_{EV}^{SDR} is the TOA reflectance before the correction of polarization effect; C_{pl} is the polarization correction factor (defined by Equation (7)); a and δ are the prelaunch characterized polarization amplitude and phase angle, respectively (see Section 3.2); q is the ratio between Q and I; and u is the ratio between U and I. m_{12} and m_{13} are the Muller matrix components, which can be derived using prelaunch-measured polarization amplitude and phase angle. Figure 7 shows the HAM side-, detector-, and scan angle-dependent m_{12} and m_{13} terms for NOAA-20 M1.

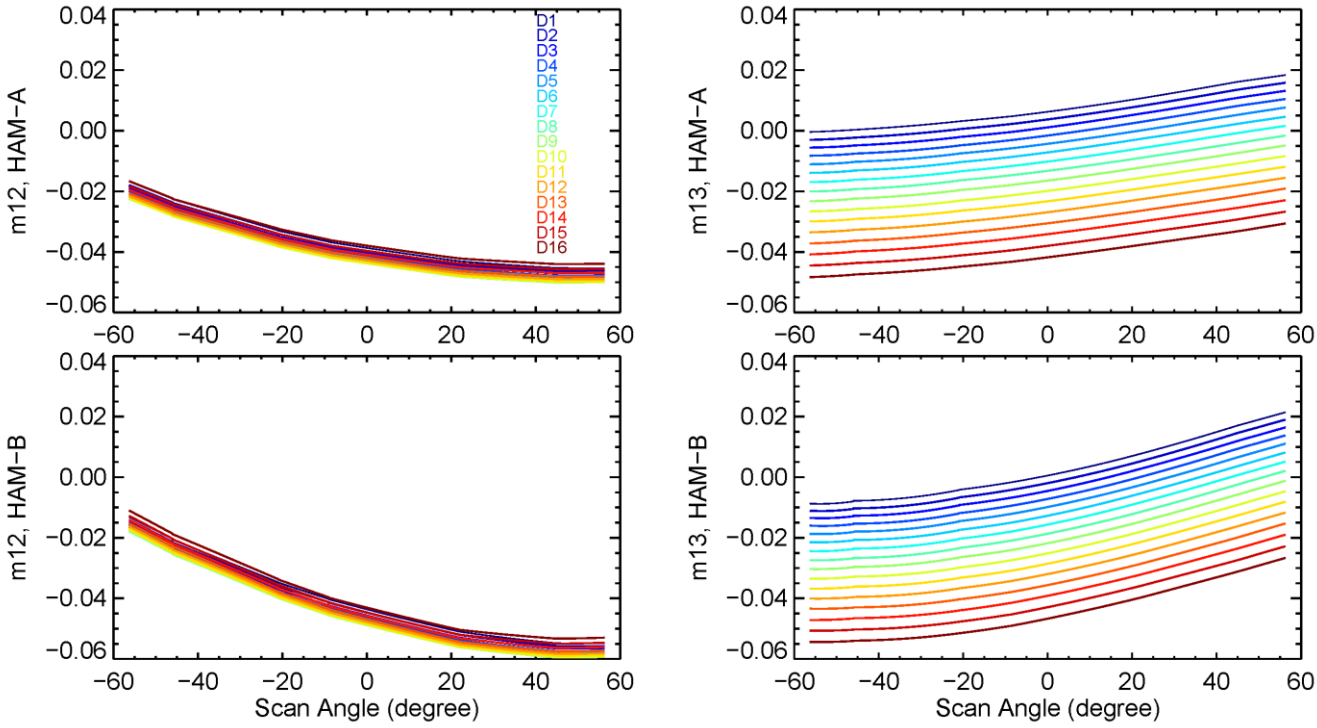

Figure 7. NOAA-20 VIIRS M1 detector- and HAM-side-dependent m_{12} (left panel) and m_{13} (right panel) terms as a function of the scan angle, derived using prelaunch characterized polarization amplitude and phase angle.

3.4. Impacts of Polarization Correction on M1 Striping

As described in Section 3.1, the Raleigh scattering-induced polarization effects over clear-sky ocean vary with solar and viewing geometries. Theoretically, the polarization-induced striping in the NOAA-20 M1 SDRs might be up to ~4%. However, the actual striping observed is smaller due to a unique feature of VIIRS called "bow-tie deletion", which trims the M-band and I-band edge detector pixels in the along-track direction to exclude some overlapping observations at higher scan angles [24,25]. For M1, observations from detectors 1–2 and 15–16 are deleted in the SDR products at absolute scan angles higher than 31.59°; observations from detectors 3–4 and 13–14 are deleted at absolute scan angles higher than 44.68°. Moreover, these bow-tie detection zones show larger polarization sensitivity and higher DoLP compared to non-bow-tie deletion zones (near nadir zones), especially for the bow-tie zones toward the end of each scan (see Figure 3d). In this study, we focus on analyzing striping using near nadir AOIs only. Bow-tie deletion zones were excluded to avoid confusion.

Figure 8a shows an example of a clear-sky ocean scene with significant striping. A NOAA operational M1 granule on 9 January 2024 20:36 UTC (latitude: 29.27°, longitude: −116.95°) was used. The normalized cumulative histograms for individual detectors and HAM sides are shown in Figure 8b. The AOI averaged SA is 30.3°, DoLP is 0.59, and the striping index is ~3.4% (derived using Equation (2)). Figure 8c shows reflectance ratios between individual detectors and the band-averaged value for the two HAM sides. The reflectance over this scene is strongly detector dependent, with reflectance increases with detector index numbers (1–16, production order). Moreover, the reflectance is also weakly HAM-side dependent, with HAM-B reflectance about 1% higher than that of HAM-A (see Figure 8c).

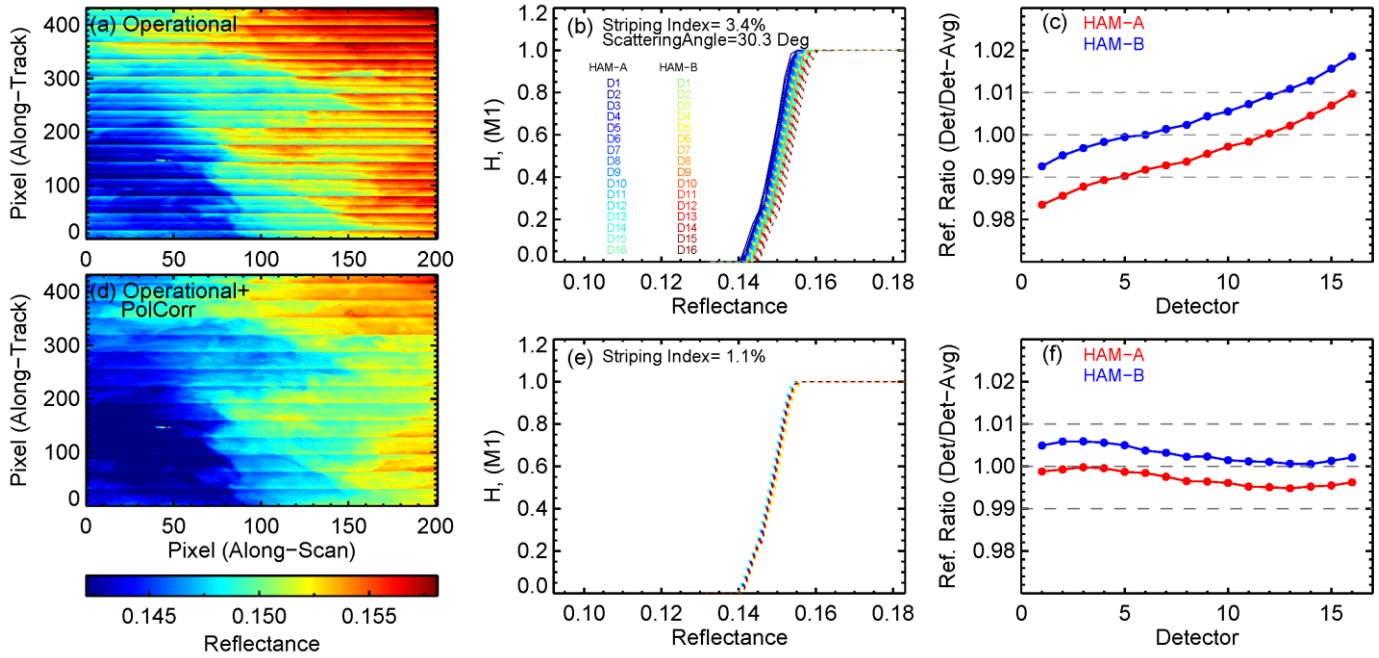

Figure 8. NOAA-20 M1 striping over a clear-sky ocean scene on 9 January 2024 20:36 UTC: (**a**) operational SDR image; (**b**) HAM-side and detector-level reflectance divergence in the operational SDR; (**c**) operational reflectance ratios between individual detectors and band-averaged value; (**d**–**f**) are similar to (**a**–**c**), but after applying the polarization correction. The gray horizontal dash lines in (**c**,**f**) mark reflectance ratio values of 0.99, 1.00, and 1.01, to assist understanding only.

Figure 8d,e show residual striping after applying the polarization correction method presented in Section 3.3. It can be observed that striping was reduced from 3.4% (see Figure 8b) to ~1.1% (see Figure 8e). The detector-dependent striping was largely removed after applying the polarization correction. The residual detector-dependent striping is likely caused by the in-homogeneity of the scene and/or calibration errors. Although HAM side-dependent striping was also reduced after the polarization correction, there still remains a residual HAM-side-dependent striping, with HAM-B reflectance ~0.5% higher than that of HAM-A.

Figure 9 shows the impacts of polarization correction on another NOAA-20 M1 clear-sky ocean scene (23 September 2018 06:12 UTC, latitude: −16.28°, longitude: 112.09°, Indian Ocean, West Coast of Australia). The polarization effect over this case is much smaller than the previous case, with AOI averaged SA of ~18.1°. Before the polarization correction, the striping index is ~1.5% (see Figure 9b). The striping was reduced slightly (by ~0.2%) after applying the polarization correction (see Figure 9e), but consistent with the small polarization effect predicted by the SA. A residual HAM side-dependent striping was also observed, with HAM-B reflectance ~0.5% higher than those of HAM-A. The residual HAM side-dependent striping observed in this case is generally consistent with that shown in the previous case (see Figures 8f and 9f).

In this study, the impacts of polarization correction on NOAA-20 M1 striping over clear-sky ocean scenes were analyzed using more cases during 2018–2024 under various scan angle and SA conditions. Results are summarized in Table 2. VIIRS observations over sun-glint regions are not used by ocean color retrieval; therefore, sun-glint affected scenes were not studied in this paper. While the polarization effect-induced striping varies, the residual striping after the polarization correction generally agrees among these cases. Results from these cases suggest that there exists a HAM side-dependent striping that is not likely caused by the polarization effect. Instead, it may be caused by errors in the on-orbit radiometric calibration, which will be studied in the next section.

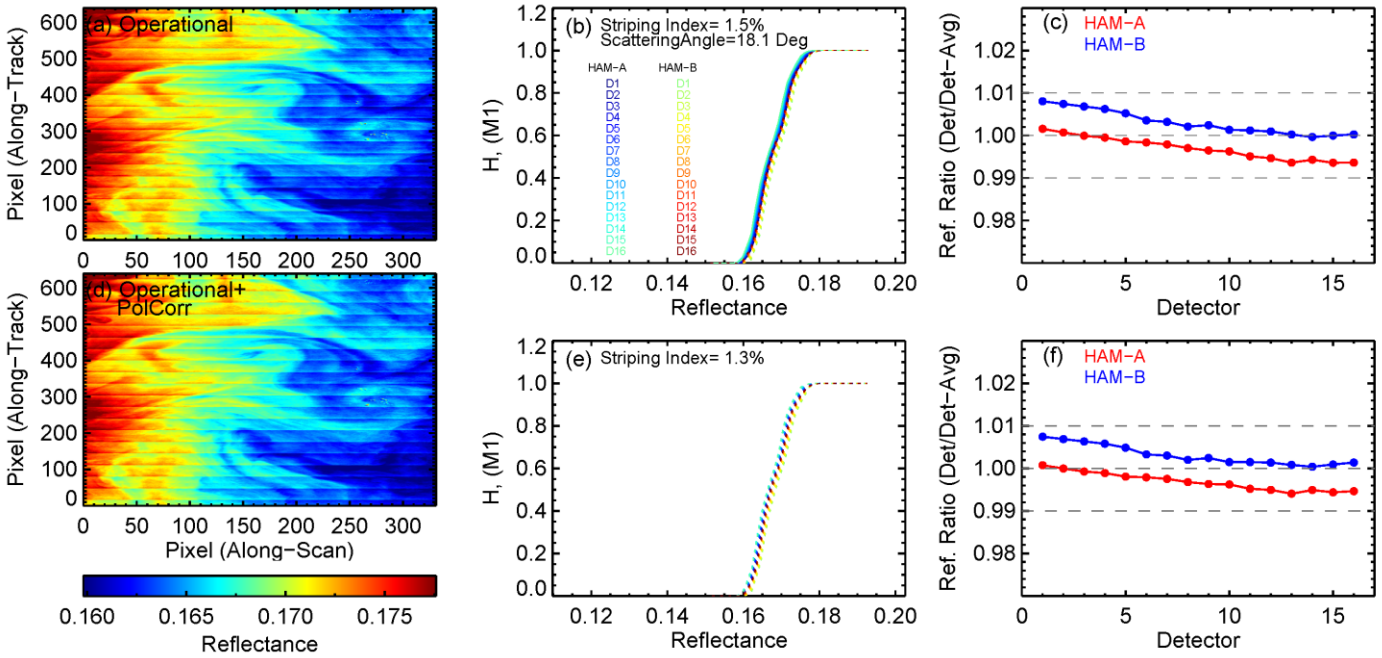

Figure 9. Similar to Figure 8, but for a NOAA-20 M1 clear-sky ocean scene on 23 September 2018 06:12 UTC (Indian Ocean, West Coast of Australia): (**a**) operational SDR image; (**b**) HAM-side and detector-level reflectance divergence in the operational SDR; (**c**) operational reflectance ratios between individual detectors and band-averaged value; (**d**–**f**) are similar to (**a**–**c**), but after applying the polarization correction. The gray horizontal dash lines in (**c**,**f**) mark reflectance ratio values of 0.99, 1.00, and 1.01, to assist understanding only.

Table 2. Summary of the impacts of polarization correction and DCC-based striping correction on NOAA-20 M1 striping over clear-sky ocean. Note: Cases #2 and #9 are also shown in Figures 8, 9, 12 and 13.

	Observation Time (UTC)	Lat/ Lon (°)	Scan Angle (°)	Scattering Angle (°)	DoLP	Striping Index (%)		
						Operational	After Polarization Correction	After DCC-Based Striping Correction + Polarization Correction
1	02/04/2018 00:16	45.49/ −172.52	2.9	60.0	0.52	2.7	1.3	1.1
2	09/23/2018 06:12:50	−16.28/ 112.09	−12.5	18.1	0.07	1.5	1.3	0.8
3	10/14/2018 21:49	44.13/ −132.89	−11.2	48.5	0.32	2.1	1.0	0.9
4	01/20/2019 21:06	22.98/ −116.11	−20.0	26.6	0.21	1.3	1.1	1.0
5	02/22/2020 20:01	19.95/ −106.84	27.2	10.4	0.41	1.9	1.3	0.9
6	02/19/2021 21:38	27.72/ −125.13	−20.0	23.7	0.16	1.2	1.1	0.9
7	10/19/2022 22:02	40.84/ −135.97	−5.9	48.9	0.34	2.4	1.2	0.9
8	7/14/2023 11:26	33.70/ 28.75	−28.0	18.4	0.03	1.4	1.3	0.8
9	1/9/2024 20:36	29.27/ −116.95	24.6	30.3	0.59	3.4	1.1	0.6

Table 2. *Cont.*

	Observation Time (UTC)	Lat/ Lon (°)	Scan Angle (°)	Scattering Angle (°)	DoLP	Striping Index (%)		
						Operational	After Polarization Correction	After DCC-Based Striping Correction + Polarization Correction
10	1/9/2024 20:36	30.00/ −113.63	3.7	50.2	0.41	3.4	1.5	1.1
11	1/26/2024 11:51	35.51/ 17.69	−4.3	51.7	0.38	2.5	1.6	1.2
12	1/26/2024 11:51	35.53/ 16.45	2.3	52.5	0.43	3.0	1.3	0.9
13	03/15/2024 21:40	34.42 −125.96	−24.0	22.2	0.14	1.1	1.2	0.8
14	03/15/2024 21:43	42.22/ −129.35	−17.6	33.2	0.21	1.5	1.2	0.8

4. Characterizing Radiometric Calibration Errors-Induced Striping in M1 SDR

Besides the polarization effect-induced striping, errors in the on-orbit radiometric calibration, such as those due to the nonuniform degradations of SD and/or errors in positional dependence in the prelaunch-measured SD reflectance [14,26], may also introduce striping in the VIIRS SDRs. The on-orbit radiometric calibration errors-induced striping in the VIIRS RSB SDRs can be characterized using observations over homogeneous Earth targets that are not significantly affected by the polarization effect, such as DCCs and desert sites [15,27,28]. However, VIIRS RSB radiometric calibrations are detector, HAM-side, and gain-stage dependent. The performance of calibration may vary with radiance levels due to non-linear response. M1 is a dual-gain band. Clear-sky ocean observations are in high gain, while observations over DCCs and desert sites are in low gain. Further investigations are needed to analyze if the striping correction factors estimated over bright vicarious targets are effective over clear-sky ocean scenes.

In this section, we first estimated NOAA-20 M1 HAM-side- and detector-dependent striping correction factors using DCC observations. Then, the DCC-based correction factors were verified over the Libya-4 desert site, the radiance level of which is between the bright DCC targets and the dark ocean scenes. Finally, the impacts of DCC-based striping factors over clear-sky ocean were presented.

4.1. DCC-Based Striping Correction Factors

DCCs are extremely cold clouds over the Inter-Tropical Convergence Zone. They are bright and stable Earth targets with near-Lambertian reflectance in the VisNIR spectrum. VIIRS DCCs can be identified using the thermal band centered at ~11 μm (VIIRS M15). Previously, we have developed the DCC method for VIIRS for evaluating the RSB long-term calibration stability [5,15,29] and detector-level degradations [15]. Results show that no significant detector-level degradation was observed in the operational NOAA-20 RSB SDRs, different from S-NPP. Moreover, no significant striping was observed over DCCs in all VisNIR SDRs. However, the HAM-side-dependent calibration divergence was not considered in our previous study [15]. Mu et al. [27] analyzed the HAM-side- and detector-dependent striping in the NASA NOAA-20 VIIRS level 1b data over DCCs, independently calibrated by the NASA VIIRS science team and processed by the Land Science Investigator-led Processing System.

In this study, the DCC identification criteria were used as those in our previous studies [5,15,29]:

1. Latitude: $\pm 25^{\circ}$;
2. TB11 (M15, center wavelength 10.7 μm) $\leq$ 205 K;
3. Standard deviation of TB11 for the subject pixel and its eight adjacent pixels $\leq$ 1 K;
4. Standard deviation of reflectance for subject pixel and its eight adjacent pixels $\leq$ 3%;
5. SZA $\leq 40^{\circ}$;
6. VZA $\leq 35^{\circ}$.

After the DCCs were identified, HAM-side and detector-level monthly DCC mean reflectance time series values were first calculated. Then, time, detector, and HAM side-dependent striping correction factors ($f(t, ham, det)$), the inverse of detector- and HAM-side-level radiance divergences, were derived using Equation (11):

$$f(t, ham, det) = \frac{R_{DCC,\ band-averaged}(t)}{R_{DCC,\ indiviual}(t, ham, det)} \tag{11}$$

where t is time; $R_{DCC,\ band-averaged}(t)$ is the band averaged monthly mean DCC reflectance at time t; and $R_{DCC,\ indiviual}(t, ham, det)$ is the HAM-side- and detector-dependent monthly mean DCC reflectance at time t. Unlike when using DCC time series for long-term calibration stability analyses, no anisotropic effect or annual cycle correction is needed for the striping analyses. DCC striping correction factors were further smoothed using a moving average with a window size of 12 months. $f(t, ham, det)$ is designed as a scaling factor that can be simply multiplied to the F-factors (VIIRS RSB calibration factor) for operational implementation. Moreover, this method is designed to reduce striping in the SDRs only, and averaged scene radiance will not be altered.

Figure 10 compares DCC-based striping correction factors for (a) considering detector-dependent striping only (combining detector level data from the two HAM sides) and (b) considering both HAM-side- and detector-dependent striping. It can be observed that M1 striping over DCCs is ~0.4% when only detector dependency is considered, due to the fact that detector-level divergences for the two HAM sides are mostly canceled out by each other. After considering both detector and HAM-side dependencies, the NOAA-20 M1 striping is larger, at ~1.1%. In addition, the NOAA-20 M1 HAM-side- and detector-dependent striping is nearly constant from February 2018 to present. The HAM-side-dependent striping is much smaller in other NOAA-20 VisNIR bands, with M2 showing relatively larger striping (~0.25%). Sun et al. [16] suggested a ~1% of HAM-side-dependent relative calibration error in the NOAA operational M1 SDRs, based on a clear-sky ocean scene on 4 February 2018. In the operational processing, HAM-B F-factors are 0.4% higher than HAM-A for both low gain and high gain since the beginning of the NOAA-20 mission (see Section 2.1 and Figure 2b). Results from this study indicate that HAM-A radiance should be increased by up to ~0.25%, while HAM-B radiance should be lowered by ~0.25% (see Figure 10b). On the one hand, the HAM-side-dependent striping found in this study is generally consistent with [14], which suggests that the striping is likely due to the error in the prelaunch-measured HAM's reflectivity extrapolated to the SD view angle. On the other hand, the striping in the operational NOAA-20 VisNIR SDRs is nearly constant overtime, which is different from [14]. NOAA and NASA NOAA-20 VIIRS RSB SDRs are calibrated independently by the NOAA and NASA VIIRS radiance science teams. In the NOAA operational processing, the detector level RSB calibration has not been updated using SD observations since 27 April 2018. Instead, band averaged calibration updates were applied based on vicarious calibration techniques (lunar calibration and the DCC technique). Unlike the gradual increase of striping the NASA L1B product, the striping in the NOAA operational M1 SDR has been relatively stable over time.

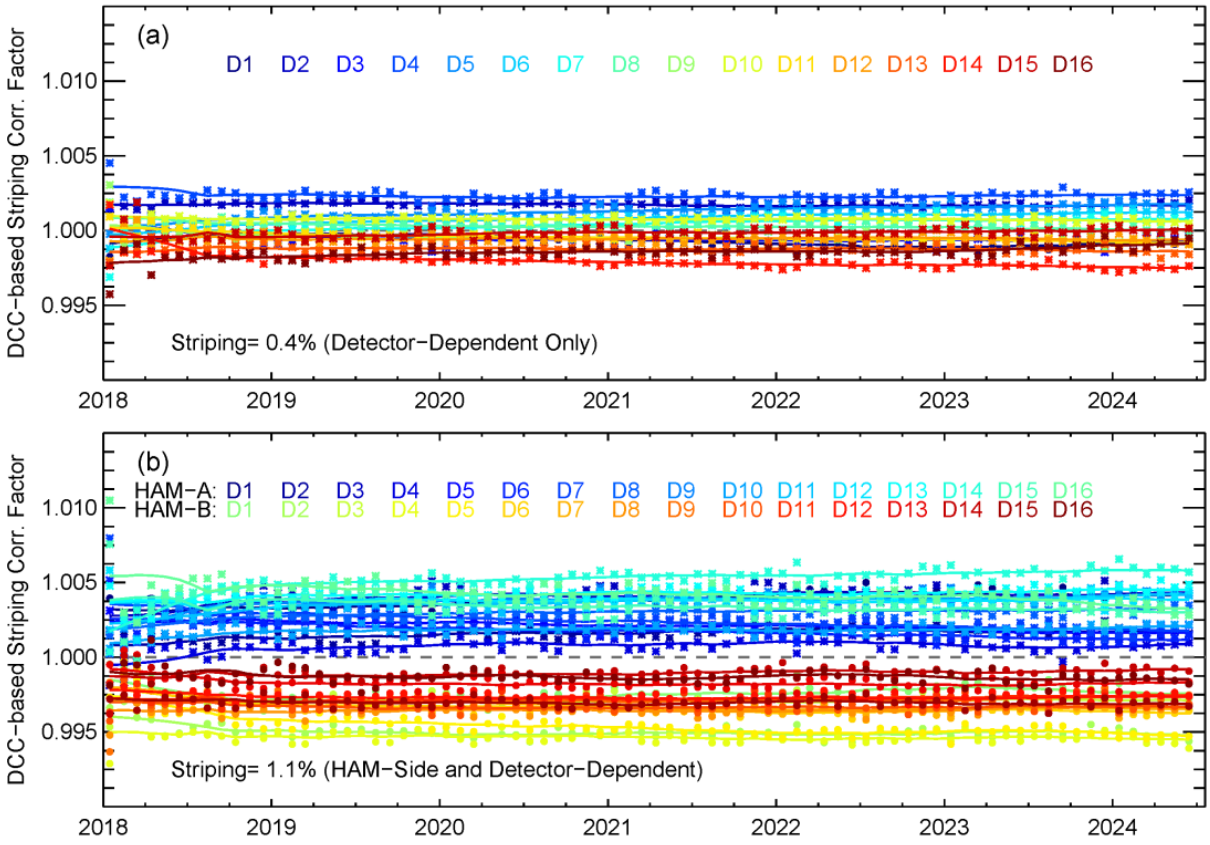

Figure 10. Comparison of NOAA-20 M1 DCC-based striping correction factors for (**a**) considering detector-dependent striping only and (**b**) considering both HAM-side- and detector-dependent striping.

4.2. Impacts of DCC-Based Striping Correction over the Libyan-4 Site

DCCs are very bright at the VIIRS M1 wavelength (0.41 μm), with a typical radiance of ~500 W/(m^2 sr μm) [30]. The DCC-based striping correction factors might not work well at lower radiance levels due to the non-linear response. In this study, the impacts of HAM-side- and detector-dependent striping correction factors were first evaluated over the Libya-4 desert site, a well-known vicarious calibration site for evaluating VisNIR calibration performance. Different from DCCs and clear-sky ocean, the Libya-4 site has a medium level of radiance, ~100 W/(m^2 sr μm). Figure 11 compares the striping before and after the DCC-based striping correction, over a near nadir homogenous area at the Libya-4 site (30 March 2024, 11:32 UTC, SA = 26.4°). Before the correction, the striping index is ~1.2%, with an obvious HAM-side-dependent striping (see Figure 11c). After the correction, the striping index was reduced to ~0.9%, and the HAM-side-dependent striping was effectively reduced (see Figure 11f). We also evaluated the effectiveness of DCC-based striping correction using another granule at the Libya-4 site during the early NOAA-20 mission (27 February 2018). Results indicate that the striping over this case was also reduced. The residual striping may be caused by the polarization effect and scene inhomogeneities. Note that the polarization correction method given in Section 3.3 is only effective over clear-sky ocean. No polarization correction was applied over the Libya-4 site. Although the TOA reflectance is not dominated by the Rayleigh scattering anymore over desert, the impact of polarization over this site is generally larger than that over DCCs. The impact of polarization over desert sites will be studied in the future.

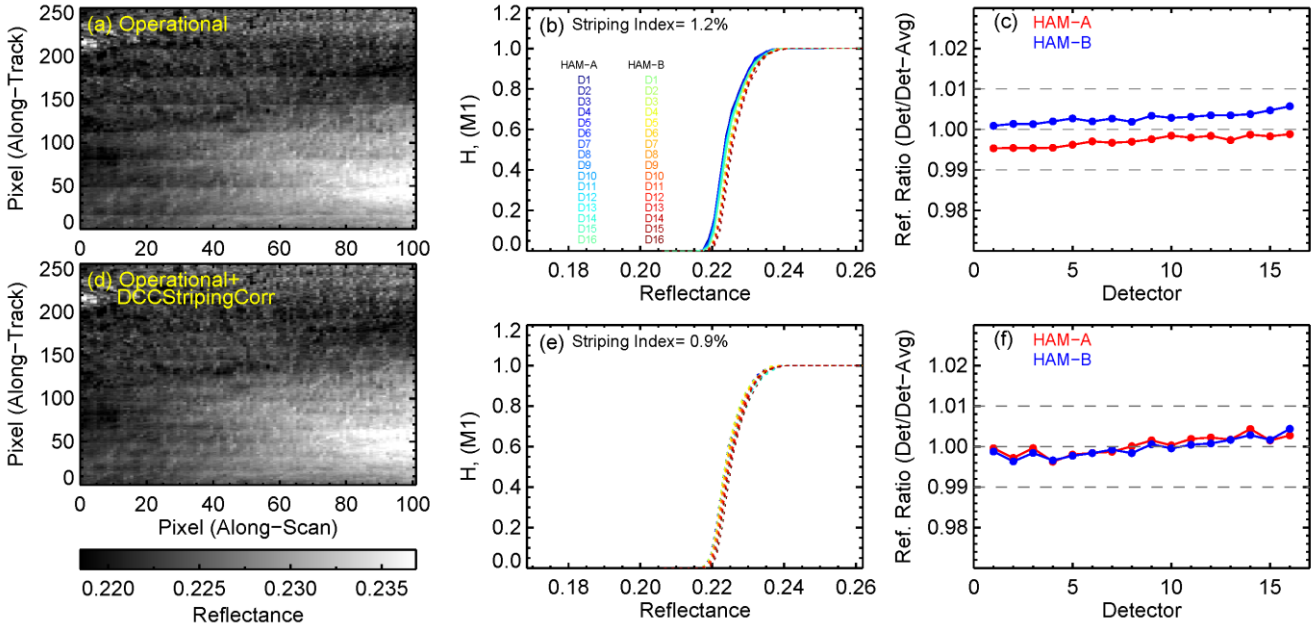

Figure 11. Impacts of DCC-based striping correction factors for NOAA-20 M1 over the Libyan-4 desert site (30 March 2024, 11:32 UTC): (**a**) operational SDR image; (**b**) HAM-side and detector-level reflectance divergence in the operational SDR; (**c**) operational reflectance ratios between individual detectors and band-averaged value; (**d**–**f**) are similar to (**a**–**c**), but after applying the DCC-based striping correction. The gray horizontal dash lines in (**c**,**f**) mark reflectance ratio values of 0.99, 1.00, and 1.01, to assist understanding only.

5. Impacts of DCC-Based Striping Correction and Polarization Correction over Clear-Sky Ocean

In this section, the DCC-based striping correction is applied to clear-sky ocean scenes, followed by the polarization correction. The two corrections are independent of each other. Figure 12 shows the impacts of both corrections on the Pacific Coast case (see Figure 8). For this case, residual striping is further reduced from ~1.1% (after polarization correction only, see Figure 8e) to ~0.6% (after applying both DCC-based striping correction and polarization correction). The HAM-side-dependent striping is mostly removed, while the detector-dependent striping is also slightly reduced (see Figure 12c).

For the Indian Ocean case (see Figure 13), the residual striping is further reduced from ~1.3% (after polarization correction only, see Figure 9e) to ~0.8% (after applying both DCC-based striping correction and polarization correction, see Figure 13b). The HAM-side-dependent striping is effectively reduced, while the detector-dependent striping is also slightly reduced (see Figure 13c) compared to applying polarization correction only.

Table 2 summarizes the impacts of polarization correction and the DCC-based striping on NOAA-20 M1 for all cases analyzed in this study, including observations time, latitude/longitude, scattering angle, DoLP, and striping indices for no correction, after polarization correction, and after both polarization correction and DCC-based striping correction. Our results suggest that both the polarization correction method and the DCC-based striping correction used in this study are effective. After applying the polarization correction to M1 clear-sky ocean scenes, residual HAM-side- and detector-dependent striping were similar to those observed over higher radiance level scenes (DCCs and the Libya-4 site). The DCC-based striping correction factors can effectively reduce the HAM-side- and detector-dependent striping by ~0.5% at all radiance levels. Results from the study also indicate that the prelaunch-measured polarization sensitivity is able to explain the observed striping over clear-sky ocean, after the HAM-side- and detector-dependent striping due

to the errors in SD calibration is corrected. Long-term time series of striping indices at representative scan angle and scattering angle (or DoLP) conditions will be more valuable for evaluating the stability of NOAA-20 M1 on-orbit polarization sensitivity. However, M1 striping over clear-sky ocean is strongly dependent on solar and sensor view geometries and scan angles. It is very challenging to collect sufficient homogeneous clear-sky ocean scenes for reliable time series analyses because of the un-predictable cloud occurrences. Due to time limitations, we will further study this topic in the future.

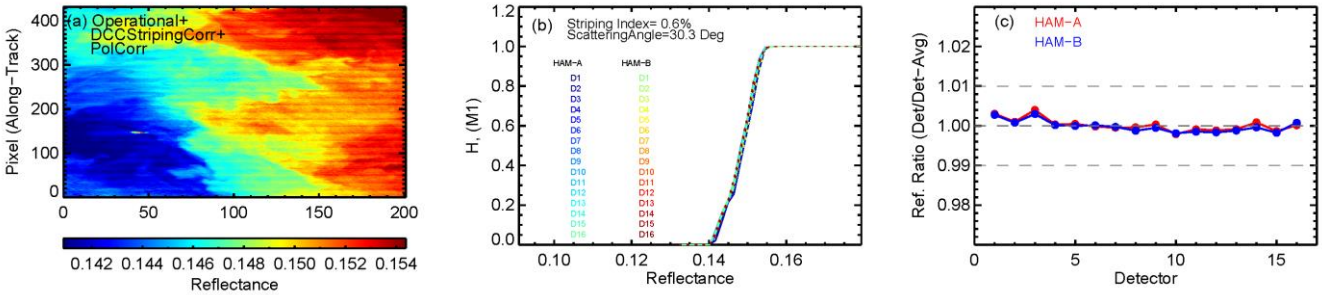

Figure 12. Similar to Figure 8, but after applying both DCC-based striping correction and polarization correction: (**a**) SDR image; (**b**) HAM-side and detector-level reflectance divergence; (**c**) reflectance ratios between individual detectors and band-averaged value. The gray horizontal dash lines in (**c**) mark reflectance ratio values of 0.99, 1.00, and 1.01, to assist understanding only.

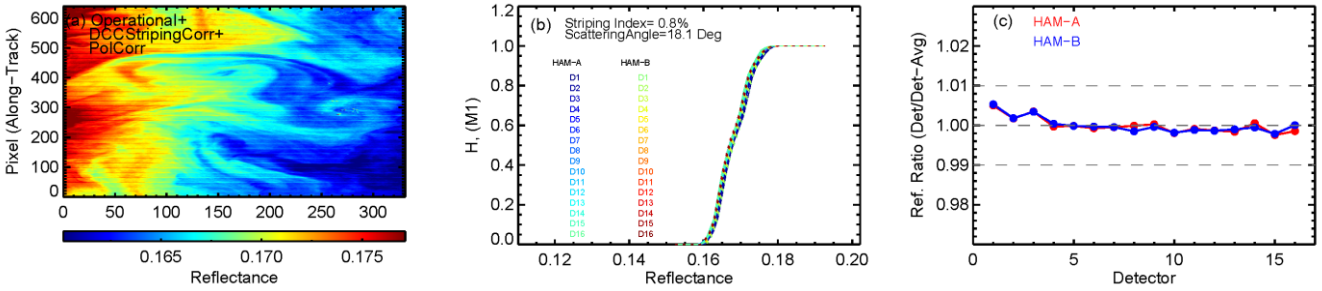

Figure 13. Similar to Figure 9, but after applying both DCC-based striping correction and polarization correction: (**a**) SDR image; (**b**) HAM-side and detector-level reflectance divergence; (**c**) reflectance ratios between individual detectors and band-averaged value. The gray horizontal dash lines in (**c**) mark reflectance ratio values of 0.99, 1.00, and 1.01, to assist understanding only.

While the polarization correction used in this study works only over clear-sky ocean, the DCC-based striping correction factors can be applied operationally. A 0.5% of error in the M1 SDR may introduce 5% of error in the ocean color retrieval [31]. The radiometric calibration uncertainty requirement of VIIRS RSBs is 2%. Moreover, NOAA-20 VIIRS RSB is the GSICS calibration reference [8]. The DCC-based M1 striping correction factors are worth implementing in the NOAA operational processing and reprocessing, to improve the quality of NOAA-20 VIIRS M1 SDRs at all radiance levels.

This study focuses on NOAA-20 M1 only; the polarization correction and the DCC-based striping correction methods presented in this study are also potentially useful for investigating the root causes for other VIIRS VisNIR bands that exhibit significant striping over clear-sky ocean. It is worth noting that scene-dependent striping was also observed in some S-NPP shorter wavelength solar bands over ocean in the NOAA operational processing. Although the S-NPP VIIRS striping issue is out of the scope of this paper, it will be valuable to investigate if it is caused by the polarization effect only or if calibration errors also contribute to the striping over clear-sky ocean.

6. Conclusions

This study investigated the potential root causes of striping in the operational NOAA-20 M1 SDR over clear-sky ocean. Two major factors were analyzed: (1) polarization effect-induced striping and (2) on-orbit radiometric calibration errors-induced striping. Prelaunch test results indicate that NOAA-20 VIIRS M1 exhibits larger polarization sensitivity, up to ~6.4%. The impact of polarization effect on M1 striping over clear-sky ocean was investigated using 6SV radiative transfer simulations and a polarization correction method similar to that used by the NOAA ocean color team. Our results indicate that the prelaunch-measured polarization sensitivity and the polarization correction method can effectively reduce striping over clear-sky ocean scenes, especially over zones with significant Rayleigh scattering-induced polarization effects. No significant change in NOAA-20 M1 polarization sensitivity was observed based on the 2018–2024 cases analyzed in this study. Moreover, a consistent HAM-side-dependent residual striping (~0.5%) becomes more obvious after the polarization correction. The residual HAM-side-dependent striping is likely caused by the imperfect on-orbit radiometric calibration, at least partially.

The radiometric calibration errors-induced striping in the NOAA-20 M1 SDRs was first characterized over the DCCs. Different from clear-sky ocean, DCCs are bright, homogenous, pseudo-invariant Earth targets, which are not significantly affected by the polarization effect. The derived DCC-based HAM-side- and detector-dependent striping correction factors indicate that nearly constant HAM-side- and detector-dependent striping over time, on the order of 1.0%, may exist in the operational M1 SDRs. The DCC-based striping correction factors were first tested using the Libya-4 site (with a mid-level of radiance). Results show that striping is reduced from 1.2% to 0.9%. Finally, the DCC-based striping correction factors were evaluated using clear-sky ocean scenes. Results based on multiple cases indicate that the striping over clear-sky ocean can be effectively reduced from 1.5–3.4% to 0.6–1.2% after applying the DCC-based striping correction and the polarization correction.

Different from the polarization correction that is only effective over clear-sky ocean dominated by the Rayleigh Scattering radiance, the DCC-based striping correction factors work at all NOAA-20 M1 radiance levels and can be deployed operationally to improve the quality of NOAA-20 M1 SDRs. While this study focuses on NOAA-20 M1 only, the methodologies developed can be used to analyze other VIIRS VisNIR bands that exhibit significant striping over clear-sky ocean, such as S-NPP VIIRS shorter wavelength VisNIRs.

Author Contributions: Conceptualization, W.W. and C.C.; methodology, W.W., C.C. and X.S.; software, W.W.; validation, W.W.; formal analysis, W.W.; investigation, W.W.; resources, W.W., C.C. and X.S.; data curation, W.W.; writing—original draft preparation, W.W.; writing—review and editing, C.C., S.B. and X.S.; visualization, W.W.; supervision, C.C.; project administration, W.W.; funding acquisition, W.W., C.C. and X.S. All authors have read and agreed to the published version of the manuscript.

Funding: This study is partially supported by NOAA/NESDIS/STAR and the NOAA grants NA19NES4320002 and NA24NESX432C0001 (Cooperative Institute for Satellite Earth System Studies-CISESS) at the University of Maryland/ESSIC.

Data Availability Statement: The NOAA-20 VIIRS SDRs are available from the Comprehensive Large Array-data Stewardship System (CLASS, www.class.noaa.gov, latest accessed on 17 December 2024). The MERRA-2 reanalyzes data used in this study are available from the NASA Goddard Space Flight Center Distributed Active Archive Center (GSFC DAAC). The VIIRS prelaunch polarization sensitivity test data are restricted to VIIRS radiance science teams only.

Conflicts of Interest: Slawomir Blonski was employed by the company of Global Science and Technology. The remaining authors declare that the research was conducted in the absence of any commercial or financial relationships that could be construed as a potential conflict of interest.

References

1. Cao, C.; Xiong, J.; Blonski, S.; Liu, Q.; Uprety, S.; Shao, X.; Bai, Y.; Weng, F. Suomi NPP VIIRS sensor data record verification, validation, and long-term performance monitoring. *J. Geophys. Res. Atmos.* **2013**, *118*, 11664–11678. [CrossRef]
2. Cao, C.; De Luccia, F.J.; Xiong, X.; Wolfe, R.; Weng, F. Early on-orbit performance of the Visible Infrared Imaging Radiometer Suite onboard the Suomi National Polar-Orbiting Partnership (S-NPP) satellite. *IEEE Trans. Geosci. Remote Sens.* **2014**, *52*, 1142–1156. [CrossRef]
3. Cao, C.; Blonski, S.; Wang, W.; Uprety, S.; Shao, X.; Choi, J.; Lynch, E.; Kalluri, S. NOAA-20 VIIRS on-orbit performance, data quality, and operational Cal/Val support. In Proceedings of the SPIE Asia-Pacific Remote Sensing, Honolulu, HI, USA, 24–26 September 2018; Volume 107810K.
4. Choi, T.; Cao, C.; Blonski, S.; Wang, W.; Uprety, S.; Shao, X. NOAA-20 VIIRS Reflective Solar Band Postlaunch Calibration Updates Two Years In-Orbit. *IEEE Trans. Geosci. Remote Sens.* **2020**, *58*, 7633–7642. [CrossRef]
5. Wang, W.; Cao, C. Evaluation of NOAA-20 VIIRS Reflective Solar Bands Early On-Orbit Performance Using Daily Deep Convective Clouds Recent Improvements. *IEEE J. Sel. Top. Appl. Earth Obs. Remote Sens.* **2020**, *13*, 3975–3985. [CrossRef]
6. Wang, W.; Cao, C.; Blonski, S.; Shao, X.; Choi, T.; Uprety, S.; Zhang, B. Comparison of NOAA and NASA Reprocessed VIIRS Solar Band SDR/Level 1b Products over Deep Convective Clouds. Presented at the EUMETSAT Meteorological Satellite Conference, Virtual, 20–24 September 2021.
7. Choi, T.; Cao, C.; Blonski, S.; Shao, X.; Wang, W. NOAA-20 VIIRS On-orbit Reflective Solar Band Radiometric Calibration Five-Year Update. *IEEE Trans. Geosci. Remote Sens.* **2024**, *62*, 1000610. [CrossRef]
8. Doelling, D.; Cao, C.; Xiong, J. GSICS recommends NOAA-20 VIIRS as reflective solar band (RSB) calibration reference. *GSICS Q.* **2021**, *14*, 2–4.
9. Oudrari, H.; McIntire, J.; Xiong, X.; Butler, J.; Ji, Q.; Schwarting, T.; Lee, S.; Efremova, B. JPSS-1 VIIRS Radiometric Characterization and Calibration Based on Pre-Launch Testing. *Remote Sens.* **2016**, *8*, 41. [CrossRef]
10. Oudrari, H.; McIntire, J.; Xiong, X.; Butler, J.; Lee, S.; Lei, N.; Schwarting, T.; Sun, J. Prelaunch Radiometric Characterization and Calibration of the S-NPP VIIRS Sensor. *IEEE Trans. Geosci. Remote Sens.* **2015**, *53*, 2195–2210. [CrossRef]
11. Moyer, D.; McIntire, J.; Xiong, X. Pre-Launch Polarization Assessment of JPSS-2 VIIRS VNIR Bands. *Remote Sens.* **2022**, *14*, 5547. [CrossRef]
12. Sun, J.; Xiong, X.; Waluschka, E.; Wang, M. *SNPP VIIRS Polarization Sensitivity Analysis*; National Oceanic and Atmospheric Administration: Silver Spring, MD, USA, 2016.
13. Moyer, D.; McIntire, J.; Young, J.; McCarthy, J.K.; Waluschka, E.; Xiong, X.; Luccia, F.J.D. JPSS-1VIIRS Prelaunch Polarization Testing and Performance. *IEEE Trans. Geosci. Remote Sens.* **2017**, *55*, 2463–2476. [CrossRef]
14. Lei, N.; Li, S.; Wilson, T.; Mu, Q.; Twedt, K.; Geng, X.; Xiong, X. Earth reflectance image striping mitigation for NOAA-20 VIIRS visible and near-infrared bands. In Proceedings of the SPIE Optical Engineering + Applications 2024, San Diego, CA, USA, 1–5 August 2024; p. 1314314.
15. Wang, W.; Cao, C.; Shao, X.; Blonski, S.; Choi, T.; Uprety, S.; Zhang, B.; Bai, Y. Evaluation of 10-Year NOAA/NASA Suomi NPP and NOAA-20 VIIRS Reflective Solar Band (RSB) Sensor Data Records (SDR) over Deep Convective Clouds. *Remote Sens.* **2022**, *14*, 3566. [CrossRef]
16. Sun, J.; Wang, M.; Jiang, L.; Xiong, X. NOAA-20 VIIRS polarization effect and its correction. *Appl. Opt.* **2019**, *58*, 6655–6665. [CrossRef]
17. Gordon, H.R.; Du, T.; Zhang, T. Atmospheric correction of ocean color sensors: Analysis of the effects of residual instrument polarization sensitivity. *Appl. Opt.* **1997**, *36*, 6938–6948. [CrossRef] [PubMed]
18. Wang, M. A refinement for the Rayleigh radiance computation with variation of the atmospheric pressure. *Int. J. Remote Sens.* **2005**, *26*, 5651–5663. [CrossRef]
19. Wang, M. The Rayleigh lookup tables for the SeaWiFS data processing: Accounting for the effects of ocean surface roughness. *Int. J. Remote Sens.* **2002**, *23*, 2693–2702. [CrossRef]
20. Global Modeling and Assimilation Office (GMAO). *MERRA-2 inst1_2d_asm_Nx: 2d, 1-Hourly, Instantaneous, Single-Level, Assimilation, Single-Level Diagnostics 0.625 x 0.5 Degree V5.12.4 (M2I1NXASM)*; National Aeronautics and Space Administration (NASA), Ed.; Goddard Space Flight Center Distributed Active Archive Center (GSFC DAAC): Greenbelt, MD, USA, 2015.
21. Sromovsky, L.A. Effects of Rayleigh-scattering polarization on reflected intensity: A fast and accurate approximation method for atmospheres with aerosols. *Icarus* **2005**, *173*, 284–294. [CrossRef]
22. Roujean, J.-L.; Leroy, M.; Deschamps, P.-Y. A bidirectional reflectance model of the Earth's surface for the correction of remote sensing data. *J. Geophys. Res. Atmos.* **1992**, *97*, 20455–20468. [CrossRef]
23. Meister, G.; Kwiatkowska, E.J.; Franz, B.A.; Patt, F.S.; Feldman, G.C.; McClain, C.R. Moderate-Resolution Imaging Spectroradiometer ocean color polarization correction. *Appl. Opt.* **2005**, *44*, 5524–5535. [CrossRef] [PubMed]
24. VIIRS Geolocation ATBD. *Joint Polar Satellite System (JPSS) VIIRS Geolocation Algorithm Theoretical Basis Document (ATBD)*; Goddard Space Flight Center: Greenbelt, MD, USA, 2011.

25. Cao, C.; Xiong, X.J.; Wolfe, R.; DeLuccia, F.; Liu, Q.M.; Blonski, S.; Lin, G.G.; Nishihama, M.; Pogorzala, D.; Oudrari, H.; et al. *Visible Infrared Imaging Radiometer Suite (VIIRS) Sensor Data Record (SDR) User's Guide*; NOAA/NESDIS: Silver Spring, MD, USA, 2017.
26. Lei, N.; Xiong, X.; Mu, Q.; Li, S.; Chang, T. Positional Dependence of SNPP VIIRS Solar Diffuser BRDF Change Factor: An Empirical Approach. *IEEE Trans. Geosci. Remote Sens.* **2021**, *59*, 8056–8061. [CrossRef]
27. Mu, Q.; Wu, A.; Xiong, X.; Angal, A. Assessment of SNPP VIIRS RSB detector-to-detector differences using deep convective clouds and deserts. *J. Appl. Remote Sens.* **2020**, *14*, 018503. [CrossRef]
28. Li, S.; Xiong, X.; Lei, N. S-NPP and N20 VIIRS RSB bands detector-to-detector calibration differences assessment using a homogeneous ground target. In Proceedings of the SPIE Optical Engineering + Applications 2020, Online, 24–28 August 2020.
29. Wang, W.; Cao, C. Monitoring the NOAA Operational VIIRS RSB and DNB Calibration Stability Using Monthly and Semi-Monthly Deep Convective Clouds Time Series. *Remote Sens.* **2016**, *8*, 32. [CrossRef]
30. Chen, Y.; Iturbide-Sanchez, F.; Tremblay, D.; Tobin, D.; Strow, L.; Wang, L.; Mooney, D.L.; Johnson, D.; Predina, J.; Suwinski, L.; et al. Reprocessing of Suomi NPP CrIS Sensor Data Records to Improve the Radiometric and Spectral Long-Term Accuracy and Stability. *IEEE Trans. Geosci. Remote Sens.* **2022**, *60*, 5502714. [CrossRef]
31. Gordon, H.R.; Voss, K.J. *MODIS Normalized Water-Leaving Radiance Algorithm Theoretical Basis Document*; Version 5; University of Miami: Coral Gables, FL, USA, 2004.